Impact of dispersion forces on matter-wave scattering near a dielectric disk

Max Könne,[1] Robert Bennett,[1] Thomas Reisinger,[2] and Stefan Yoshi Buhmann[1,3]
[1]*Physikalisches Institut, Albert-Ludwigs-Universität Freiburg, Hermann-Herder-Str. 4, D-79104 Freiburg i. Br., Germany*
[2]*Institute of Nanotechnology, Karlsruhe Institute of Technology, Hermann-von-Helmholtz-Platz 1, D-76344 Karlsruhe, Germany*
[3]*Freiburg Institute for Advanced Studies, Albert-Ludwigs-Universität Freiburg, Albertstr. 19, D-79104 Freiburg i. Br., Germany*
(Received 12 May 2017; published 25 July 2017)

The influence of the Casimir-Polder potential upon matter-wave scattering near a dielectric disk is considered. We employ a rescaled Dyson series in order to take into account the disk geometry, and compare this with a previously used approach based on the proximity-force approximation. In the latter approach one uses a simplified potential that is sharply switched on in the region of the disk. This intrinsically neglects edge and saturation effects. We show that under appropriate conditions the previous simpler model works very well for the calculation of the phase accumulated along the full path of the particle due to approximate cancellations of the errors. We present specific results for experimentally relevant scenarios, namely indium atoms or deuterium molecules interacting with a silicon nitride or silicon dioxide disk. Finally we compare our calculations to the analytically solvable problem of an infinitely thin perfectly reflecting disk, finding the expected qualitative agreement.

DOI: 10.1103/PhysRevA.96.013626

I. INTRODUCTION

Matter-wave diffraction around material objects is a striking demonstration of the wave-particle duality of nature. The earliest examples of diffraction of massive particles were the famous electron diffraction experiments of Davisson [1,2], whose work started a long chain of experiments aiming to do the same with ever-increasing particle masses. This has led to, for example, diffraction of fullerenes [3] and porphyrin derivates [4] using gratings of various types. A long-term goal of these experiments is to test if the predictions of the quantum-mechanical superposition principle apply to particles of increasingly macroscopic size and mass [5,6], or if any modifications of quantum theory are required to describe macroscopic systems [7].

Here we investigate a particular class of diffraction experiments—the "Poisson spot" (sometimes called the spot of Arago) interferometer, where diffraction of any type of wave around a cylindrically symmetric object results in an on-axis bright spot. The matter-wave version of this experiment [8] avoids some of the problems that appear in the grating experiments discussed above (e.g., blocking of the grating, or the need for wavelength selection). However, there is an inevitable contribution to the phase of the matter wave from the Casimir-Polder potential [9] arising from interaction between the object and the diffracting matter-wave beam, which can affect the intensity of the spot and the placement of fringes. Calculation of Casimir-Polder potentials is in general very complicated, as they depend on the electromagnetic field subject to boundary conditions imposed by the geometry of the object. This can only be worked out analytically without approximations for the very simplest geometries (plane, cylinder, sphere; see, for example, [10]), with anything more complicated being tackled through numerical methods. If one restricts to the nonretarded regime (which is most relevant for matter-wave experiments), the potential near an infinitely thin, conducting disk can be calculated analytically [11]. However, the most important region in such diffraction experiments is when the atom is passing the edge of the disk, so the assumption of an infinitely thin disk is not necessarily a good one there. For these reasons Casimir-Polder effects have been accounted for in Ref. [12] using a relatively simple model of the experiments of Ref. [8], where the potential is considered to be zero everywhere except in the plane of the disk, as shown in Fig. 1. In the previously used version of this approximation the potential in the "switched-on" region was taken to be that for a simple half-space (as shown in the inset of Fig. 1), which corresponds to the assumption that only atoms passing very close to the disk will have their phases noticeably altered. In this study we will investigate in detail the validity of this approach, which we shall refer to as the "proximity-force approximation" (PFA), well known from Casimir physics [13]. It will be shown that the geometrical part of the PFA (the assumption of a sharp switch-on) is a good approximation to reality, while the size of the switched-on potential (found from considering the disk to be an infinite half-space) is not. This will lead us to use a hybrid of the PFA and a Dyson series in the susceptibility of the disk, where the Casimir-Polder potential near the plane of a disk (not a half-space) is sharply switched on.

II. BASIC THEORY

In this section we will outline a general derivation for the Casimir-Polder (CP) interaction for a dielectric disk and a single ground-state atom and show that it reduces to well-known results in asymptotic cases. We will follow the approach of Ref. [14], which is based on the formalism introduced in Ref. [15], now known as macroscopic quantum electrodynamics (QED). There the system of the electromagnetic field coupled to absorbing media can be quantized in one of several equivalent ways, leading to the following expression for the macroscopic QED electric field operator:

$$\hat{\mathbf{E}}(\mathbf{r}) = \frac{i}{c^2}\sqrt{\frac{\hbar}{\pi\varepsilon_0}}\int d^3\mathbf{r}'\int_0^\infty d\omega\,\omega^2\sqrt{\mathrm{Im}\varepsilon(\mathbf{r},\omega)} \times \mathbf{G}(\mathbf{r},\mathbf{r}',\omega)\cdot\hat{\mathbf{f}}(\mathbf{r}',\omega) + \mathrm{H.c.}, \quad (1)$$

where $\hat{\mathbf{f}}(\mathbf{r},\omega)$ is a bosonic field operator corresponding to the fundamental excitations of the combined matter-field system

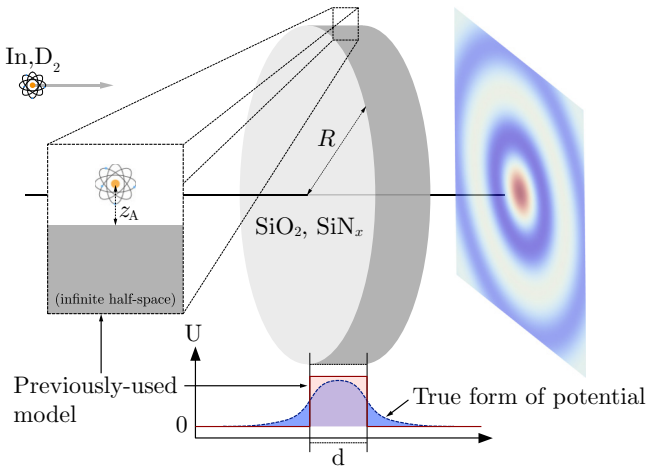

FIG. 1. Schematic of the considered setup and illustration of the improvement our model makes over a previously used one.

and $\mathbf{G}(\mathbf{r},\mathbf{r}',\omega)$ is the Green's tensor that solves

$$\nabla \times \nabla \times \mathbf{G}(\mathbf{r},\mathbf{r}',\omega) - \varepsilon(\mathbf{r},\omega)\frac{\omega^2}{c^2}\mathbf{G}(\mathbf{r},\mathbf{r}',\omega) = \delta(\mathbf{r}-\mathbf{r}'), \quad (2)$$

where $\varepsilon(\mathbf{r},\omega)$ is the position and frequency-dependent permittivity of the system.

We begin from the expression for the CP potential for an isotropically polarized atom in terms of the Green's tensor $\mathbf{G}(\mathbf{r},\mathbf{r}',\omega)$ derived in Ref. [16],

$$U(\boldsymbol{r}_\mathrm{A}) = \frac{\mu_0\hbar}{2\pi}\int_0^\infty d\xi\,\xi^2\alpha(i\xi)\mathrm{tr}[\mathbf{G}^\mathrm{S}(\boldsymbol{r}_\mathrm{A},\boldsymbol{r}_\mathrm{A},i\xi)], \quad (3)$$

where $\mathbf{G}^\mathrm{S}$ is the scattering part of the Green's tensor, i.e., that which depends on the geometry of dielectric bodies. The quantity $\alpha(i\xi)$ is the degeneracy-weighted atomic ground-state polarizability, given by

$$\alpha(i\xi) = \frac{2}{3\hbar}\sum_{j\neq 0}\frac{2J_j+1}{2J_0+1}\frac{\omega_{0j}d_{0j}^2}{\omega_{0j}^2+\xi^2}, \quad (4)$$

where ω_{0j} is the transition frequency between the ground state and the jth excited state and d_{0j} is the dipole transition moment between those states. The factor $(2J_j+1)/(2J_0+1)$ accounts for the possibly different degeneracies of the ground and excited states, whose total angular momenta are denoted J_0 and J_j, respectively.

A. Approximating the Casimir-Polder potential

The Green's tensor $\mathbf{G}^\mathrm{S}(\boldsymbol{r}_\mathrm{A},\boldsymbol{r}_\mathrm{A},i\xi)$ includes all the information about the scattering properties of the object at hand, whatever shape it is. However, the Green's tensor is known analytically only for very few geometries (bulk medium, infinite plane, infinite cylinder, sphere and layered versions thereof), and is in particular not known for our system of a finite-thickness disk. Therefore approximate methods are needed. Here we expand the Green's tensor in a Dyson series about the vacuum Green's tensor $\mathbf{G}^{(0)}(\boldsymbol{r},\boldsymbol{r}',\omega)$ with coupling parameter $\chi(\mathbf{r},\omega) = \varepsilon(\mathbf{r},\omega)-1$, which is the susceptibility of the medium. One finds for the whole Green's tensor $\mathbf{G}$ (not just its scattering part) the recursive equation:

$$\mathbf{G}(\boldsymbol{r},\boldsymbol{r}',\omega) = \mathbf{G}^{(0)}(\boldsymbol{r},\boldsymbol{r}',\omega) + \frac{\omega^2}{c^2}\int d^3s\,\chi(s,\omega) \times \mathbf{G}^{(0)}(\boldsymbol{r},\boldsymbol{s},\omega)\cdot\mathbf{G}(\boldsymbol{s},\boldsymbol{r}',\omega), \quad (5)$$

from which solutions to arbitrary order in χ can be generated. The vacuum Green's tensor $\mathbf{G}^{(0)}$ is known analytically:

$$\mathbf{G}^{(0)}(\boldsymbol{r},\boldsymbol{r}',\omega) = -\frac{c^2e^{i\omega\rho/c}}{4\pi\omega^2\rho^3}\left\{\left[1-i\frac{\omega\rho}{c}-\left(\frac{\omega\rho}{c}\right)^2\right]\mathbf{I} + \left[3-3i\frac{\omega\rho}{c}-\left(\frac{\omega\rho}{c}\right)^2\right]\boldsymbol{e}_\rho\otimes\boldsymbol{e}_\rho\right\} - \frac{c^2}{3\omega^2}\delta(\boldsymbol{\rho}), \quad (6)$$

where $\rho = |\boldsymbol{\rho}| = |\mathbf{r}-\mathbf{r}'|$, $\boldsymbol{e}_\rho$ is a unit vector along the direction of $\boldsymbol{\rho}$ and $\otimes$ denotes the outer product. It is useful to define the "regular part" $\mathbf{H}^{(0)}(\boldsymbol{r},\boldsymbol{r}',\omega)$ of the vacuum Green's tensor via

$$\mathbf{G}^{(0)}(\boldsymbol{r},\boldsymbol{r}',\omega) = -\frac{c^2}{3\omega^2}\delta(\boldsymbol{\rho}) + \mathbf{H}^{(0)}(\boldsymbol{r},\boldsymbol{r}',\omega). \quad (7)$$

The Dyson equation can then be re-expressed as

$$\mathbf{G}(\boldsymbol{r},\boldsymbol{r}',\omega) = \mathbf{G}^{(0)}(\boldsymbol{r},\boldsymbol{r}',\omega) + \frac{\omega^2}{c^2}\int d^3s\,\frac{\chi(\mathbf{s},\omega)}{1+\frac{1}{3}\chi(\mathbf{s},\omega)}\mathbf{H}^{(0)}(\boldsymbol{r},\boldsymbol{s},\omega)\cdot\mathbf{G}(\boldsymbol{s},\boldsymbol{r}',\omega). \quad (8)$$

The advantage of this is that the new perturbation parameter $\chi(\mathbf{s},\omega)/[1+{}^1\!/_3\chi(\mathbf{s},\omega)]$ does not diverge for the case of a metal disk (with its large χ). We then solve the new Dyson equation in the usual iterative way, finding

$$\mathbf{G}(\boldsymbol{r},\boldsymbol{r}',\omega) = \mathbf{G}^{(0)}(\boldsymbol{r},\boldsymbol{r}',\omega) + \sum_{K=1}^{\infty}\frac{\omega^{2K}}{c^{2K}}\int d^3s_1\frac{\chi(\boldsymbol{s}_1,\omega)}{1+\frac{1}{3}\chi(\boldsymbol{s}_1,\omega)}\cdots\int d^3s_K\frac{\chi(\boldsymbol{s}_K,\omega)}{1+\frac{1}{3}\chi(\boldsymbol{s}_K,\omega)}\mathbf{H}^{(0)}(\boldsymbol{r},\boldsymbol{s}_1,\omega)\cdot\mathbf{H}^{(0)}(\boldsymbol{s}_1,\boldsymbol{s}_2,\omega)\cdots\mathbf{H}^{(0)}(\boldsymbol{s}_K,\boldsymbol{r}',\omega). \quad (9)$$

Restricting to leading order corrections ($K=1$), we find for the Dyson-series derived CP potential U_D,

$$U_\mathrm{D}(\boldsymbol{r}_\mathrm{A}) = -\frac{\mu_0\hbar}{2\pi c^2}\int_0^\infty d\xi\,\xi^4\alpha(i\xi)\int d^3s\,\frac{\chi(\boldsymbol{s},i\xi)}{1+\frac{1}{3}\chi(\boldsymbol{s},i\xi)}\mathrm{Tr}[\mathbf{H}^{(0)}(\boldsymbol{r}_\mathrm{A},\boldsymbol{s},i\xi)\cdot\mathbf{H}^{(0)}(\boldsymbol{s},\boldsymbol{r}_\mathrm{A},i\xi)]. \quad (10)$$

After inserting the vacuum Green's tensor (6) and carrying out the trace, the potential becomes

$$U_{\rm D}(\boldsymbol{r}_{\rm A}) = -\frac{\hbar}{16\pi^3\epsilon_0}\int_0^\infty d\xi\alpha(i\xi)\int d^3s\,\frac{\chi(\boldsymbol{s},i\xi)}{1+\frac{1}{3}\chi(\boldsymbol{s},i\xi)}\frac{e^{-2\xi\frac{\rho}{c}}}{\rho^6}\left[3+6\left(\frac{\rho\xi}{c}\right)+5\left(\frac{\rho\xi}{c}\right)^2+2\left(\frac{\rho\xi}{c}\right)^3+\left(\frac{\rho\xi}{c}\right)^4\right], \tag{11}$$

where now $\boldsymbol{\rho} = \boldsymbol{r}_{\rm A} - \boldsymbol{s}$.

For explicit calculations we will consider the more physically relevant limit near-field (nonretarded) limit, which is defined by the transition wavelength being much larger than the atom-body separation ($\omega_j z_{\rm A}/c \gg 1$). In terms of Eq. (11), this corresponds to taking $e^{-2\frac{\rho\xi}{c}} \simeq 1$ and also neglecting terms of order $\rho\xi/c$ or higher in the polynomial in the second line. Furthermore we assume that the material body has a homogenous permittivity and is described by a volume $\mathbf{V}$:

$$\chi(\boldsymbol{s},i\xi) = \chi(i\xi)\mathbf{I}(\boldsymbol{s}), \quad \text{with} \quad \mathbf{I}(\boldsymbol{s}) = \begin{cases} 1 \text{ for } \mathbf{s}\in\mathbf{V} \\ 0 \text{ otherwise.}\end{cases}$$

This restricts the s integral in (11), leading to the final form of the CP potential,

$$\begin{aligned} U_{\rm D}(\boldsymbol{r}_{\rm A}) &= -\frac{3\hbar}{16\pi^3\epsilon_0}\int_0^\infty d\xi\alpha(i\xi)\frac{\chi(i\xi)}{1+\frac{1}{3}\chi(i\xi)}\int_{\mathbf{V}} d^3s\frac{1}{\rho^6} \\ &= -C_6\int_{\mathbf{V}} d^3s\frac{1}{\rho^6}, \end{aligned} \tag{12}$$

with

$$C_6 \equiv \frac{3\hbar}{16\pi^3\epsilon_0}\int_0^\infty d\xi\alpha(i\xi)\frac{\chi(i\xi)}{1+\frac{1}{3}\chi(i\xi)}. \tag{13}$$

This is the Hamaker approach [17] to the calculation of atom-body interactions, where the body is approximated as being made up of a large number of uncorrelated atoms.

There are two limits of this potential which are of interest to estimate the quality of later results. First there is the limit where the atom is so close to the disk that the latter can be approximated as a half-space, in which case the s integral $\int_{\mathbf{V}} d^3s\rho^{-6}$ in (12) becomes elementary with result $\pi/(6z_{\rm A}^3)$, giving for the "Dyson-half-space" potential,

$$U_{\rm DHS}(z_{\rm A}) = -\frac{C_{3\rm DHS}}{z_{\rm A}^3}, \tag{14}$$

with $C_{3\rm DHS} = \frac{\pi}{6}C_6$. As the notation suggests, it is important to distinguish the above CP potential (the nonretarded limit for an atom near a half-space described by a Dyson series) from the well-known nonretarded CP potential found through direct use of the exact half-space Green's function. The latter potential is

$$U_{\rm HS}(z_{\rm A}) = -\frac{C_{3\rm HS}}{z_{\rm A}^3}, \tag{15}$$

with

$$C_{3\rm HS} = -\frac{\hbar}{16\pi^2\epsilon_0 z_{\rm A}^3}\int_0^\infty d\xi\alpha(i\xi)\frac{\chi(i\xi)}{\chi(i\xi)+2}. \tag{16}$$

We will use this result to estimate the errors which stem from the approximations involved in making the Dyson series.

B. Phase shift due to the potential

We require one more formula, which is that for the accumulated phase of an atom (matter wave) traveling past the disk. If the atom moves along a trajectory parallel to the disk axis and subject to some general potential $U(\mathbf{r}_A)$, the collected phase is given by [8,12,18–20]

$$\phi = \int_{-\infty}^\infty dx_{\rm A}k(x_{\rm A}) = \int_{-\infty}^\infty dx_{\rm A}k_0\sqrt{1-\frac{U(\boldsymbol{r}_{\rm A})}{E_0}}. \tag{17}$$

Taking $E_0 = \hbar^2k_0^2/2m = mv_0^2/2$ as the initial and purely kinetic energy of the atom, as well as taking only the leading term in a Taylor series defined by $U(\boldsymbol{r}_{\rm A}) \ll E_0$ gives

$$\Delta\phi = -\frac{1}{\hbar v_0}\int_{-\infty}^\infty dx_{\rm A}U(\boldsymbol{r}_{\rm A}). \tag{18}$$

In our particular case, the potential is the CP potential (12). Using the PFA as shown in Fig. 1 together with the half-space potentials (14) and (15) one has trivially

$$\Delta\phi \simeq \frac{1}{\hbar v_0}\frac{C_3}{z_{\rm A}^3}\int_{-d/2}^{d/2} dx_{\rm A} = \frac{C_3 d}{\hbar v_0 z_{\rm A}^3}, \tag{19}$$

where d is the thickness of the disk and C_3 is either $C_{3\rm DHS}$ or $C_{3\rm HS}$ depending on which version of the half-space one wishes to use.

III. CASIMIR-POLDER POTENTIAL

To find the phase shift for real situations we need to calculate the corresponding explicit values of C_6 via Eq. (13) and $C_{3\rm HS}$ via Eq. (15), where the former will in turn give us $C_{3\rm DHS} = (\pi/6)C_6$. These three values will be collectively referred to as dispersion constants. The properties of the diffracting atom and the disk material enter into C_3 via the atomic polarizability $\alpha(\omega)$ and the material susceptibility $\chi(\omega)$, respectively, so in order to proceed we must obtain expressions for these.

A. Material response functions

In our calculations we consider two materials for the disk: silicon nitride (SiN_x) and silicon oxide (SiO_2), as well as two different kinds of diffracting particles, elemental indium (In) and deuterium molecules (D_2). These choices are motivated by recent and ongoing Poisson spot experiments [8,12,21].

1. Polarizabilities

The atomic or molecular polarizabilities are calculated from Eq. (4), where as many transitions as possible should be included for an accurate result. For indium there are only a few dominant transitions, but for deuterium there are numerous vibrational sublevels of the electronically excited manifolds whose contributions are of the same order, meaning that a large number of transitions were used. We list the transitions

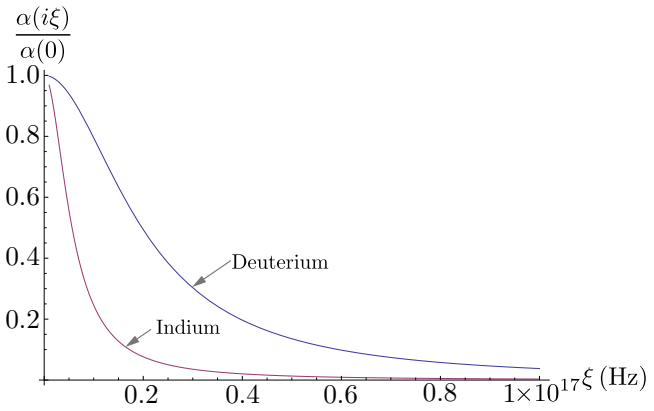

FIG. 2. Comparison of both polarizabilities as a function of (complex) frequency ξ. It can be seen that the polarizability for indium decreases much faster with frequency compared to that for deuterium.

(and their corresponding frequencies and dipole moments) for indium and deuterium in the Appendix. Then, all that remains is that these parameters have to be inserted into Eq. (4) which leads the following static (i.e., zero frequency) polarizabilities:

$$\alpha_{\mathrm{In}}(0) = 4.71 \times 10^{-40}\ \mathrm{Cm^2V^{-1}},$$
$$\alpha_{D_2}(0) = 4.98 \times 10^{-41}\ \mathrm{Cm^2V^{-1}}. \quad (20)$$

For D_2, the experimentally observed value is $\alpha_{D_2}(0) = 8.71 \times 10^{-41}\ \mathrm{Cm^2V^{-1}}$ [22], while the theoretically predicted values range from $\alpha_{D_2}(0) = 1.58 \times 10^{-41}\ \mathrm{Cm^2V^{-1}}$ to $9.10 \times 10^{-41}\mathrm{Cm^2V^{-1}}$ [23]. The frequency dependence is shown in Fig. 2, where it is seen that the polarizability decreases very rapidly for indium atoms, while for deuterium the decrease is slower.

2. Susceptibilities

For SiN_x, the susceptibility was obtained in Ref. [24], and is given by

$$\chi_{\mathrm{SiN_x}}(i\xi) = -1 + \frac{2}{\pi}\int_{\Omega_T}^{\infty} dx \frac{f\Omega\gamma(x-\Omega_T)^2}{(x^2+\xi^2)[(x^2-\Omega^2)^2+\gamma^2x^2]}, \quad (21)$$

with the following parameters (expressed as angular frequencies, i.e., they should be divided by 2π to obtain the number of cycles per second);

$$\Omega_T = 3.48 \times 10^{15}\ \mathrm{rad/s}, \quad \Omega = 1.09 \times 10^{16}\ \mathrm{rad/s},$$
$$f = 1.13 \times 10^{17}\ \mathrm{rad/s}, \quad \gamma = 1.16 \times 10^{16}\ \mathrm{rad/s}, \quad (22)$$

which leads to the static value of $\chi_{\mathrm{SiN_x}}(0) = 2.87$. A similar calculation for crystalline, uniaxial, anisotropic SiO_2 can be found in Ref. [25] (based on [26]), and results in a static value of $\chi_{\mathrm{SiO_2}}(0) = 2.9$. The dispersion constants are calculated via Eqs. (13) and (15) as well as the limit for a perfect conductor ($\varepsilon \to \infty$), with results shown in Table I.

Our results for dispersion constants for deuterium interacting with SiN_x can be directly compared to the experimental work of [27], where deuterium was diffracted from a SiN_x grating whose bars were considered large enough to be approximated by infinite half-spaces. In such a situation we obtain $C_{3\mathrm{HS}} = 3.404 \times 10^{-50}$, while [27] obtained $0.33 \pm 0.10\ \mathrm{meV\,nm^3} = (5.29 \pm 1.60) \times 10^{-50}\ \mathrm{J\,m^3}$, meaning that our result lies just slightly outside the lower error bar.

TABLE I. Dispersion constants in units of 10^{-50} $\mathrm{Jm^3}$ for indium atoms interacting with different dielectric media. Here it is easily seen that the Dyson half-space model causes an overestimate relative to the half-space model (i.e., $C_{3\mathrm{DHS}} > C_{3\mathrm{HS}}$ for all combinations of particle and disk.) The specific level of overestimation is shown in the final column and will be used later for comparison with our full integration that includes the shape of the disk. Finally we note that since $C_{3\mathrm{DHS}} = \frac{\pi}{6}C_6$ one can easily see via Eqs. (13) and (16) that in the limit of perfect conduction one will always find $C_{3\mathrm{HS}}/C_{3\mathrm{DHS}} = 2/3$, as reflected in the table.

Particle	Disk	C_6	$C_{3\mathrm{HS}}$	$C_{3\mathrm{DHS}}$	$C_{3\mathrm{HS}}/C_{3\mathrm{DHS}}$
Indium	SiN_x	32.8	14.2	17.2	0.83
Indium	SiO_2	21.1	9.78	11.04	0.89
Indium	$\varepsilon \to \infty$	91.0	31.8	47.6	0.67
Deuterium	SiN_x	7.60	3.40	3.98	0.86
Deuterium	SiO_2	5.44	2.57	2.85	0.90
Deuterium	$\varepsilon \to \infty$	33.4	11.7	17.49	0.67

B. Results

The final ingredient in determining the Casimir-Polder potential of the disk in the Dyson series picture is to carry out the integral in Eq. (12) over the volume of the disk, with the atom placed at a position $\{x_A, \rho_A\}$ as indicated in Fig. 3. There two of three integrals are solvable analytically, but because of the unmanageable size of the resulting analytical expression the whole integral was solved numerically. Our results are shown in Fig. 4 where one can clearly see the overestimation (relative to the half-space) of the potential by the Dyson series. This general feature of the Dyson series derived potentials will be accounted for using phenomenological correction factors, the results of which will be referred to as "Dyson-compensated" potentials. The contour plot Fig. 5 shows that for small distances the form of the potential is approximately rectangular, while for larger distances the shape becomes more elliptical. This is in line with the physical intuition that very

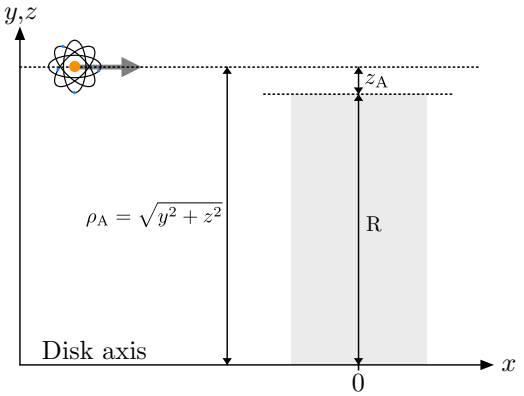

FIG. 3. The coordinate system used in our calculations of Casimir-Polder potentials.

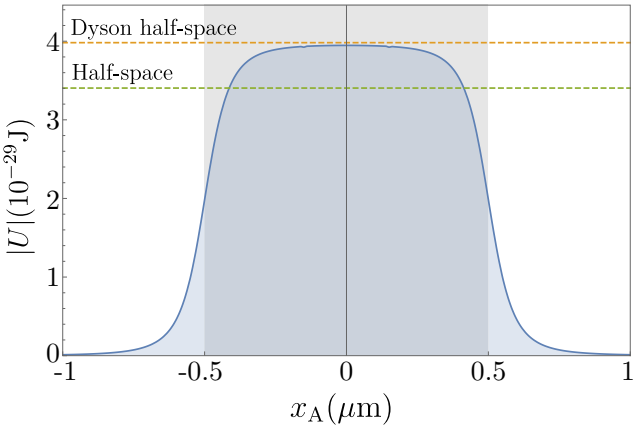

FIG. 4. Casimir-Polder potential (solid line) for a deuterium molecule at a lateral distance $\rho_A - R = 100$ nm from a SiN_x disk. The dashed lines show the potential for the Dyson half-space (14) and half-space approximated (15) for comparison. The shaded area represents the extent of the disk.

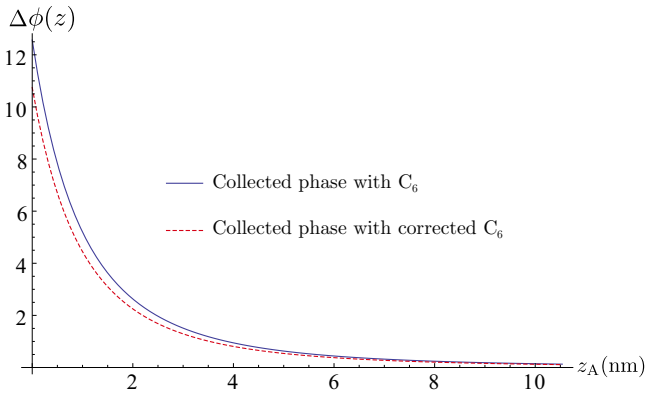

FIG. 6. (Upper curve) Collected phase [found from Eq. (18)] of a deuterium molecule moving at 1060 m/s at various distances $\rho_\mathrm{A} - r$ from the edge of a disk with the same parameters as that shown in Figs. 4 and 5. (Lower curve) The same quantity but multiplied by $C_{3\mathrm{HS}}/C_{3\mathrm{DHS}} = 0.86$ (see Table I) in order to compensate for the Dyson series overestimation.

close to the disk it should seem like a half-space, and very far away it should seem like a point particle.

IV. IMPACT ON MATTER-WAVE SCATTERING

A. Edge and saturation effects

We can now use Eq. (18) to calculate the influence of our Casimir-Polder potential results on matter-wave scattering. We assume that the atomic beam is incident perpendicular to the disk and is generated and detected sufficiently far away (relative to the size of the disk) that we can consider it to be traveling over the complete distance $x_\mathrm{A} \in (-\infty, \infty)$. The result for the phase shift with these parameters can be seen in Fig. 6 alongside its Dyson-compensated value. The latter was also compared to the phase shift in the PFA [Eq. (19)] and can be seen in Fig. 7. There, the difference is extremely small, i.e., the approximation works very well. This is to be expected as the chosen atom-disk edge distance $\rho_\mathrm{A} - R = 0.1$ μm is small compared to the radius (30 μm) and thickness (1 μm) of the disk. In other words, the disk can, to a very good approximation, be considered as a half-space with a modified dispersion constant within the PFA—the effects of the actual shape can be ignored.

This fact can be intuitively understood via Fig. 4, where we plot the Casimir-Polder potentials for the two types of half-space, as well as the disk. One can see that the full disk potential is close to zero a long way from the disk, then suddenly increases (where the half-space approximation has not yet been "switched on," so the half-space approximation is at this point underestimating the potential), intersects the point where the approximation would turn on (where the previous underestimation then switches to an overestimation), and then reaches the plateau where the half-space is a good approximation. Out

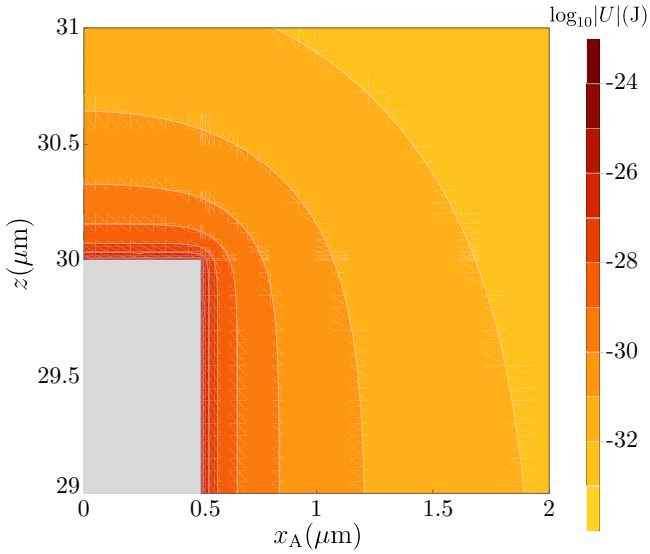

FIG. 5. Detail of the Casimir-Polder potential for a deuterium molecule near the edge of an SiN_x disk of thickness 1 μm and radius of 30 μm.

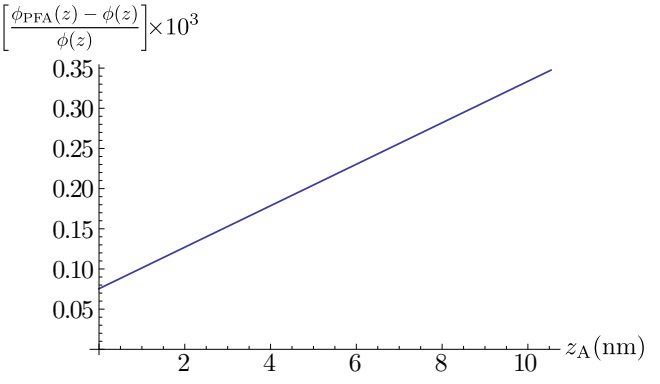

FIG. 7. The difference between the phase collected in the PFA and the Dyson-compensated phase collection from the disk modeled by Eq. (18). The difference is very small (tens of milliradians), showing that our approximation works well.

of this one can see that the underestimation on the approach to the disk roughly cancels out the overestimation due to edge effects. Effects due to incomplete saturation to the half-space plateau are negligible for the parameters used. Finally we note that of course the potential has a symmetric shape which means that the effect occurs twice, one time when the particle flies towards the disk and one time when it flies away.

B. Curvature effects

It is possible to evaluate the exact nonretarded Casmir-Polder potential near a perfectly conducting disk of zero thickness via Kelvin inversion of the problem for an infinite half-sheet [11]. The requirement of zero thickness therein means we cannot compare this directly to our Dyson series approach which relies on the disk having some finite volume. However, we can use the results of [11] to reinforce our conclusion that the shape of the disk does not matter for small distances (i.e., those dominant in matter-wave scattering) by a simple analytic calculation. Taking the results of Ref. [11] for an isotropically polarizable dipole in the plane of the disk, one finds

$$U_{\mathrm{Thin}} = \frac{d^2}{12\pi^2\epsilon_0}\frac{R\left(3\rho_{\mathrm{A}}^2+4R^2\right)}{(R-\rho_{\mathrm{A}})^3(\rho_{\mathrm{A}}+R)^3} \equiv -\frac{C_{3\mathrm{Thin}}(R)}{(\rho_{\mathrm{A}}-R)^3}, \quad (23)$$

where d is the dipole moment and a geometry-dependent dispersion coefficient $C_{3\mathrm{Thin}}(R)$ has been defined. The Casimir-Polder force in the nonretarded limit a distance $R-\rho_{\mathrm{A}}$ from a perfectly reflecting plane is

$$U_{\mathrm{PM}} = -\frac{d^2}{48\pi^2\epsilon_0(\rho_{\mathrm{A}}-R)^3} \equiv -\frac{C_{3\mathrm{PM}}}{(\rho_{\mathrm{A}}-R)^3}, \quad (24)$$

which is simply the perfectly reflecting version of Eq. (15). Taking the ratio of (23) and (24) then expanding in a Taylor series about $\rho_{\mathrm{A}} \approx R$ one finds the following result, independent of the particle species used:

$$\frac{U_{\mathrm{Thin}}}{U_{\mathrm{PM}}} = \frac{C_{3\mathrm{Thin}}(R)}{C_{3\mathrm{PM}}} = \frac{7}{2\pi} - \frac{9}{4\pi R}(\rho_{\mathrm{A}}-R) + O(\rho_{\mathrm{A}}-R)^2. \quad (25)$$

The leading term is independent of all the geometric properties of the disk—the next-to-leading term is the first geometry-dependent correction. For the parameters used in Fig. 4 ($\rho_A - R = 100$ nm, $R = 30$ μm) its magnitude is approximately 0.2% of the leading term, showing that simply taking an adjusted (but geometry-independent) value for the dispersion coefficient is enough to encapsulate most of the differences between a disk and a half-space for the parameters chosen here.

C. Effect on the relative intensity of Poisson's spot

In this section we present results from applying the predicted CP phase shift to numerical simulation of matter-wave Poisson-spot diffraction experiments [8]. The simulation is analogous to Ref. [25], where we discuss diffraction behind a spherical diffraction obstacle. The simulation is discussed in detail there, but to summarize, we solve the Fresnel-Kirchhoff diffraction integral given below, to find the intensity $|A(P)|^2$ of the wave at a point P in the shadow at a distance b behind the disk [12,28].

$$A(P) = -\frac{i}{\lambda g b}\int_0^{2\pi} d\phi \int_0^{\infty} d\rho_{\mathrm{A}}\; G(\phi,\rho_{\mathrm{A}})\rho_{\mathrm{A}} e^{i[\varphi_g(\rho_{\mathrm{A}})+\Delta\varphi_{\mathrm{CP}}(\rho_{\mathrm{A}})]}. \quad (26)$$

Here λ is the de Broglie wavelength of the matter-wave beam. g and b are the distances from source to disk and from disk to detector, respectively. $\varphi_g(\rho_{\mathrm{A}}) = \frac{\pi}{\lambda}(\frac{1}{g}+\frac{1}{b})\rho_{\mathrm{A}}^2$ is the phase shift due to the variation in path lengths from source to image points via different points in the plane of the disk. $\varphi_{\mathrm{CP}}(\rho_{\mathrm{A}})$ is the CP-induced phase shift given by Eq. (19). The aperture function $G(\phi,\rho_{\mathrm{A}})$ is used to model the diffraction obstacle, i.e., the blocking disk. It is 0 for points blocked by the disk and 1 otherwise. In order to compute the on-axis intensity for an extended source, a convolution of the point-source diffraction image with the source image is necessary. Therefore, $A(P)$ must be also evaluated for points P away from the optical axis, which we achieve by shifting the aperture function $G(\phi,\rho_{\mathrm{A}})$ appropriately. We neglect the change in the angle of the disk with the optical axis for these off-axis points. As discussed in Ref. [25], we restrict the numerical inclusion of the CP phase shift to an annular region concentric with the disk, allowing for a maximum CP phase shift of 4π and a minimal phase shift of $\pi/1000$.

In Fig. 8 we use this method to predict the relative (to the unobstructed case) on-axis intensity I_{rel} of Poisson's spot as a function of detector distance for the deuterium Poisson spot experiment described in Ref. [8]. In the experiment a supersonic beam of deuterium (D_2) with a measured terminal beam velocity of $v = 1060$ m/s (peak of velocity distribution and equivalent to a de Broglie wavelength of $\lambda = 93.5$ pm [29]) and a velocity spread of $\Delta v/v = 0.054$, was incident on a silicon-nitride disk of 60 μm in diameter and with thickness less than 1 μm. The source, which had a diameter of 50 μm, was located 1496 mm from the disk. For the figures we have assumed the two different dispersion constants derived here as well as the constant $C_{3,\mathrm{GRI}}$ measured by Grisenti *et al.* [27]. Besides the silicon-nitride disk used in the experiment we additionally present the case of a disk made from silicon dioxide which could be prepared for a future experiment. For both materials we performed the calculations for disk thicknesses of 500 nm and 1000 nm, which corresponds to the uncertainty interval of the experimental disk thickness. Finally, the graphs are compared to I_{rel} computed without any CP phase shift. Note that also in this case the relative intensity slightly increases with distance from the disk. This is due to the comparatively large source diameter and small diffraction intensities, which result in an increasingly important contribution from the shadow's outer edge. The latter adds to the on-axis peak due to the farthest off-axis source points in the extended source convolution. At smaller b the relative diffraction intensity increases sharply as expected, and the differences between the predicted intensities due to a variation of the dispersion constant become more pronounced.

In addition to the on-axis intensities we display the expected lateral distribution of the relative intensity in the shadow in Fig. 9. The assumed experimental parameters are the same as in Fig. 8, and we show the case of a realistic closest approach of

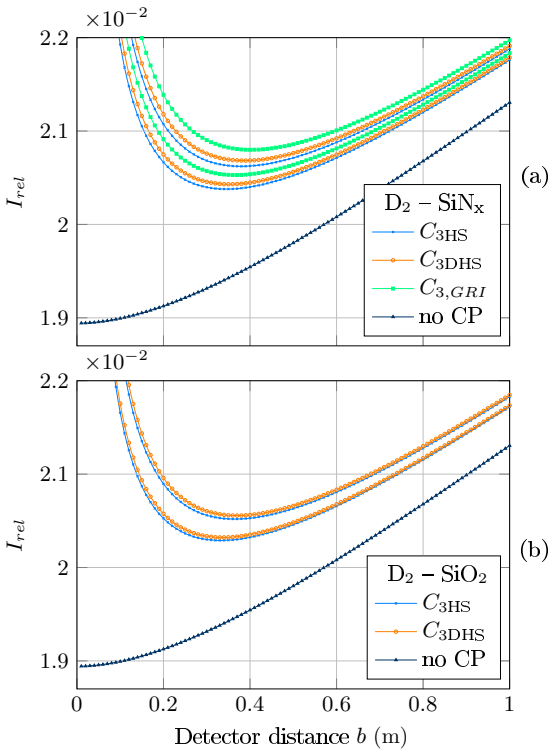

FIG. 8. Effect of the CP-induced phase shift on matter-wave diffraction. The plots show the relative on-axis intensity of Poisson's spot calculated for the experimental parameters used in Ref. [8] assuming as the diffraction obstacle (a) a silicon-nitride disk, as was used in the experiment, and (b) a silicon-dioxide disk. $I_{\rm rel}$ is given in intensity units of the undisturbed wave front (without the sphere the plot would show $I_{\rm rel} = 1$). The on-axis intensities were calculated using the two different dispersion constants given in Table I as indicated. The graph in (a) labeled as $C_{3,\rm GRI}$ was calculated using the half-space dispersion constant determined in the experiment of Ref. [27]. The thick graphs assume a disk thickness of 1 μm and the thin graphs 0.5 μm. The graph indicated with "no CP" shows the relative intensity of Poisson's spot without any phase shift due to the CP potential.

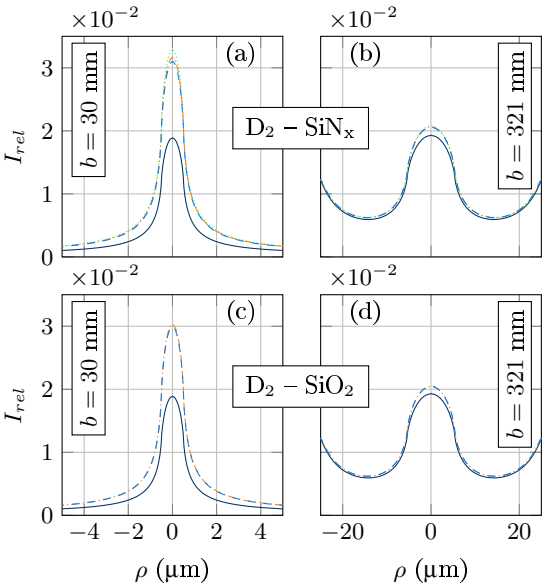

FIG. 9. Simulated lateral relative intensity for the deuterium Poisson spot experiment [8] for detector distances (a) and (c) $b = 30$ mm, and (b) and (d) $b = 321$ mm. The line styles indicate the type of CP potential used (colors analogous to Fig. 8). Dark blue solid lines, no CP potential; light blue dashed lines, $C_{3\rm HS}$; orange dashdotted lines, $C_{3\rm DHS}$; green dotted lines, $C_{3,\rm GRI}$. In (b) and (d) the difference in the simulated intensity for the different dispersion constants is not visible; a small change, mostly on axis, can be seen for the smaller detector distance.

the detector of $b = 30$ mm and the smallest detector distance used in the deuterium Poisson spot experiment of $b = 321$ mm. In the latter case it is clear that the effect of the CP-induced phase shift is nearly negligible, especially when compared to the influence of disk edge corrugation and support structure (see Fig. 10). In particular the graphs associated with the different C_3 constants overlap. However, at the smaller detector distance we expect that the predicted differences can be tested experimentally, as long as some experimental prerequisites can be met, as discussed below.

The simulations shown in Figs. 8 and 9 neglect any edge corrugation of the disk, for which a more significant reduction in Poisson spot intensity is expected at smaller b. Furthermore, any support structure of the disk that blocks the incident de Broglie waves is expected to reduce the intensity of Poisson's spot. Thus, in order to be able to compare the simulation to experiments both of these effects need to be accounted for. This we illustrate in Fig. 10. There we modify the Dyson half-space-based relative intensity simulation for the deuterium experiment using two attenuation factors that were derived and tested in Ref. [30] for light diffraction.

The factor $C_{\rm supp}$ modeling the reduction in intensity due to support bars is defined by

$$C_{\rm supp} = 1 - \frac{c_{\rm supp} n_{\rm supp} w_{\rm supp}}{2\pi R},$$

where $n_{\rm supp}$ is the number and $w_{\rm supp}$ is the width of the support bars which were 4 and 3 μm in the experiment of Ref. [8], respectively. The constant $c_{\rm supp}$ we set to 1.5 as determined in [30]. The expected attenuation due to the support structure is shown as a gray area in Fig. 10. Next, we define the factor $C_{\rm corr}$ we use for taking into account disk edge corrugation of a square wave shape and with a peak-to-peak amplitude of $\sigma_{\rm corr}$ as follows:

$$C_{\rm corr} = \begin{cases} \cos^2\left(\frac{\pi}{2}\frac{\sigma_{\rm corr}}{w_{fz}}\right) & \text{if } \sigma_{\rm corr} < w_{fz} \\ \sim 0 & \text{otherwise} \end{cases}.$$

Here, $w_{fz} = \sqrt{R^2 + \frac{\lambda g b}{(g+b)}} - R$ is the width of the Fresnel zone adjacent to the rim of the disk. In Fig. 10 the effect of increasing $\sigma_{\rm corr}$ in steps of 10 nm up to 300 nm is shown as an orange color gradient. Note that this analysis excludes any effect the corrugation has on the CP potential. The data points as measured in Ref. [8] are superimposed on the gradient including their experimental uncertainty [31]. In order to deduce the relative intensity $I_{\rm rel} = (I_{\rm PS} - I_{\rm BG})/(I_0 - I_{\rm BG})$ from the experiment it is important to measure any background intensity $I_{\rm BG}$ and subtract it from the on-axis intensity $I_{\rm PS}$ and unobstructed intensity I_0 of the beam.

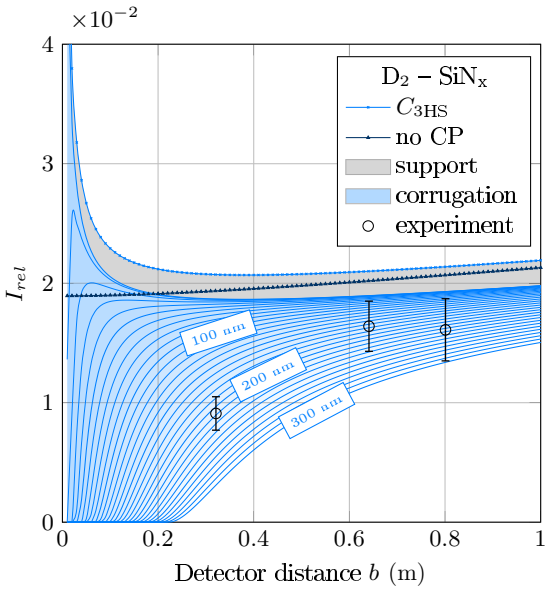

FIG. 10. Simulated relative on-axis intensity of Poisson's spot for the deuterium experiment compared to the experimental values deduced from Ref. [8]. Here we only show the result for the normal half-space dispersion constant $C_{3\mathrm{HS}}$ and a disk thickness of 1 μm, but include an estimate for the influence of the support bars that kept the disk in place (intensity reduced by area shaded in gray) and an increasing amount of disk edge corrugation (orange contour lines correspond to increases of peak-to-peak corrugation amplitude σ_{corr} in steps of 10 nm). The data points agree with a corrugation amplitude of about 200 nm.

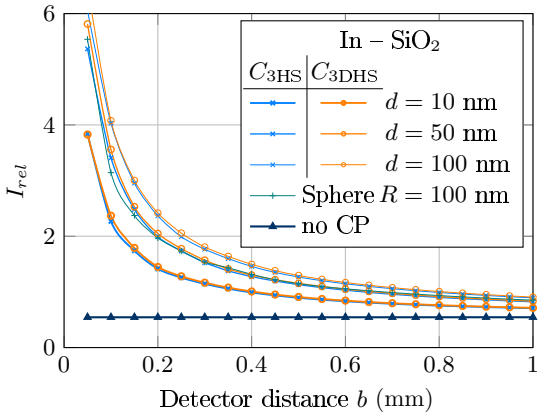

FIG. 11. Simulated relative on-axis intensity of Poisson's spot in the shadow of a silicon-dioxide disk 200 nm in diameter and indium atoms as beam species. The thickness of the disk we assume to be 10 nm, 50 nm, and 100 nm as indicated. Besides the CP interaction potential the experimental parameters (wavelength $\lambda = 6.67$ pm, source width $w_s = 20$ μm, $g = 600$ mm) are the same as for the experiment discussed in Ref. [25], where the focus is on diffraction of indium atoms at a silicon-dioxide sphere. For comparison we show the relative on-axis intensity behind a 200-nm diameter sphere, which we computed using the sphere-radius dependent dispersion constant $C_{52} = 9.365 \times 10^{-22}$ m$^{5/2}$ for the CP phase shift $\Delta\varphi_{\mathrm{CP,\,BNR}} = C_{52}/z_{\mathrm{A}}^{5/2}$ in the vicinity of a sphere introduced there.

It can be seen that the data is compatible with an edge corrugation of about 200 nm. This is less than the 300 nm included in the simulation of Ref. [8], but is also in qualitative agreement with the 250 nm determined from microscopy. This also complies with the fact that the factor C_{corr} assumes a worst case square wave corrugation and the numerical model in Ref. [8] used a fourth power sine corrugation function. The latter type of corrugation requires a larger peak-to-peak amplitude to cause the same attenuation of Poisson's spot. A contribution from CP to the intensity cannot be deduced with certainty, but we can estimate the parameters needed to perform an experiment that would allow this. First, the large uncertainty of the data values is mainly due to the large uncertainty of the background and unobstructed intensity values, which were unfortunately only determined in initial measurements with short integration times. A measurement with uncertainties of the order of 1% seems feasible in future experiments.

Second, a reduction in the disk edge corrugation to about $\sigma_{\mathrm{corr}} = 10$ nm we expect to be achievable using electron-beam lithography or focused ion beam milling. This would allow a measurement of the beam profiles shown in Fig. 9(a) or 9(b) with a limited amount of attenuation. To be able to differentiate between Dyson half-space and normal half-space dispersion constants, it should be noted that in such an experiment the distance b would have to be measured more precisely, as the expected increase in I_{rel} strongly depends on b. Finally, the reduced Poisson spot width at the smaller distance b would require a higher resolution detector to measure the on-axis intensity accurately (the detector aperture was 11 μm in the deuterium experiment). A precise knowledge of the dispersion constants for the CP interaction of deuterium with silicon nitride is also relevant for focusing of deuterium with Fresnel zone plates [32,33]. It could allow an optimization of the zone plate, for example, with regard to chromatic aberration.

Finally, we apply our results to the indium matter-wave Poisson spot experiment discussed in Ref. [25], where the diffracting object was a sphere, rather than a disk. We can find the disk thickness d_{crit} that would give the same phase shift as a sphere with the same diameter by setting our expression (19) for the accumulated phase equal to Eq. (21) of [25] which is the corresponding relation for the sphere. Solving for the disk thickness d one finds

$$d_{\mathrm{crit}} = \frac{3\pi}{4\sqrt{2}}\sqrt{R z_{\mathrm{A}}} \approx 1.7\sqrt{R z_{\mathrm{A}}}, \tag{27}$$

where R is the radius of the sphere. Taking $R = 100$ nm and a notional z_{A} of 10 nm gives $d_{\mathrm{crit}} \approx 54$ nm which fits well with the results of the full simulations shown in Fig. 11. There we show plots of the relative intensity of Poisson's spot corresponding to the two dispersion constants for the indium atom and silicon dioxide disk interaction assuming three different disk thicknesses, namely 10 nm, 50 nm, and 100 nm. This we compare to the relative intensity for a sphere with the same diameter as the disk, namely 200 nm. The relative intensity for the sphere corresponds very well to that for a disk of 50-nm thickness. The distinction between half-space and Dyson half-space Poisson-spot intensities is even less distinct than in the deuterium experiment, due to additional fluctuations of the relative intensity as a function of b. The latter occurs because the adjacent Fresnel zone in the indium experiment is of smaller width than the annular zone

in which we have to account for a CP phase shift (up to about 30 nm). In the deuterium experiment the adjacent Fresnel zone is much wider (up to about 900 nm).

V. SUMMARY

We have investigated the effect of the attractive Casimir-Polder potential on matter-wave scattering from a dielectric disk, and considered a specific example of deuterium being diffracted by SiN_x, as shown in Figs 4 and 5. We have also determined dispersion parameters for other situations of experimental interest. We have compared our results to a commonly used model (the PFA) where the potential is sharply switched from zero to its half-space value when the atom enters the plane of the disk. This comparison showed that while the Casimir-Polder potential looks quite different in the two cases, the phase shift (which is found by an integral over the potential) is largely unaffected due to approximate cancellation of errors associated with edge effects, and the smallness of errors associated with curvature and incomplete saturation. This is expected to break down if one moves further away from the disk (to the region where it looks less like a half-space), but for the experimentally motivated parameters chosen here the approximation works very well, as demonstrated in Sec. IV B where we have checked the consistency of our results by using known analytic results for an infinitesimally thin disk.

We have used the calculated dispersion constants to simulate the effect of the CP potential on the relative intensity of Poisson's spot in deuterium and indium matter-wave diffraction experiments. In particular we compare the predicted on-axis intensities for the half-space and Dyson half-space model. Furthermore, we compare the intensities to results from the deuterium experiment of Ref. [8]. An effect from the CP-induced phase shift could not be deduced from the deuterium data, but this may be possible in future experiments, the requirements of which we have also discussed.

The main conclusion of our work is that matter-wave diffraction around a disk can be accurately modeled by the sharply switched-on half-space model with a corrected dispersion constant—the actual geometric properties can be safely ignored.

ACKNOWLEDGMENTS

We thank Johannes Fiedler and Joshua Hemmerich for fruitful discussions. S.Y.B and R.B. acknowledge support from the Deutsche Forschungsgemeinschaft (Grant No. BU 1803/3-1), and S.Y.B. additionally acknowledges support from the Freiburg Institute for Advanced Studies (FRIAS) and the Research Innovation Fund of Freiburg University. T.R. acknowledges support from the Ministry of Science, Research and Art of Baden-Württemberg via a Research Seed Capital (RISC) Grant No. 33-7533-30-10/25/3, as well as the Helmholtz association.

APPENDIX: TRANSITION DATA

In this section we quote transition frequencies and dipole moments that determine the polarizability for indium (Table II) and deuterium (Tables III, IV, and V).

TABLE II. Transition frequencies and dipole moments for indium [34]. The transition starts from the ground state, whose electron configuration in its outer shell is $5s^2_{1/2}5p^1_{1/2}$. Frequencies are given in units of 10^{15} rad/s and dipole moments in units of 10^{-30} Cm.

Level j	ω_{0j}	d_{0j}
$6s^1_{1/2}$	4.591	11.2995
$5d^1_{3/2}$	6.1957	10.923
$7s^1_{1/2}$	6.838	3.201
$6d^1_{3/2}$	7.355	3.666
$8s^1_{1/2}$	7.6546	1.780
$7d^1_{3/2}$	7.8804	1.3055

TABLE III. Ground-to-first electronic excited state (with vibrational quantum number ν) transition frequencies and dipole moments for the Lyman ($X^1\Sigma^+_g - B^1\Sigma^+_u$) system of deuterium [35]. All frequencies ω_{0j} are given in units of 10^{16}rad/s, and all dipole moments d_{0j} are in units of 10^{-32} Cm.

ν	ω_{0j}	d_{0j}	ν	ω_{0j}	d_{0j}	ν	ω_{0j}	d_{0j}
0	1.71	22.75	18	2.03	150.46	36	2.36	30
1	1.73	49.51	19	2.05	139.03	37	2.38	27.44
2	1.74	80.68	20	2.07	128.01	38	2.4	25.09
3	1.76	112.95	21	2.09	117.54	39	2.41	22.94
4	1.78	143.48	22	2.11	107.7	40	2.43	20.97
5	1.8	170.16	23	2.12	98.52	41	2.45	19.24
6	1.82	191.87	24	2.14	90	42	2.47	17.7
7	1.83	207.92	25	2.16	82.13	43	2.49	16.27
8	1.85	218.33	26	2.18	74.91	44	2.51	14.91
9	1.87	223.54	27	2.2	68.28	45	2.52	13.59
10	1.89	224.15	28	2.21	62.24	46	2.54	12.27
11	1.91	221.08	29	2.23	56.72	47	2.56	11.03
12	1.92	215.04	30	2.25	51.72	48	2.58	9.67
13	1.94	206.67	31	2.27	47.17	49	2.6	7.99
14	1.96	196.73	32	2.29	43.03	50	2.61	6.06
15	1.98	185.74	33	2.31	39.28	51	2.63	2.72
16	2	174.08	34	2.32	35.88	52	2.65	2.31
17	2.02	162.28	35	2.34	32.8	–	–	–

TABLE IV. Ground-to-second electronic excited state (with vibrational quantum number ν) transition frequencies and dipole moments for the Werner ($X^1\Sigma^+_g - C^1\Pi_u$) system of deuterium [35] (notation and units the same as Table III).

ν	ω_{0j}	d_{0j}	ν	ω_{0j}	d_{0j}
0	1.87	219.27	10	2.2	116.39
1	1.91	321.49	11	2.23	95.49
2	1.94	361.38	12	2.26	78.35
3	1.97	357.62	13	2.3	64.48
4	2	329.12	14	2.33	53.18
5	2.04	289.51	15	2.36	43.94
6	2.07	247.39	16	2.39	36.23
7	2.1	207.63	17	2.43	29.63
8	2.13	172.24	18	2.46	23.38
9	2.17	141.82	–	–	–

TABLE V. Transition frequencies and dipole moments for the higher electronically excited states of deuterium [36] (notation and units the same as Tables III and IV). The vibrational quantum number of the excited state is labeled as v.

Level	v	ω_{0j}	d_{0j}	Level	v	ω_{0j}	d_{0j}	Level	v	ω_{0j}	d_{0j}	Level	v	ω_{0j}	d_{0j}
$5p\pi$	2	2.33	43.21	$14p\pi$	2	2.4	9.19	$5p\pi$	7	2.45	27.1	$5p\pi$	9	2.5	24.95
$10p\pi$	0	2.33	7.87	$15p\pi$	2	2.4	8.5	$6p\pi$	6	2.45	23.32	$13p\pi$	6	2.5	9.15
$11p\pi$	0	2.33	7.23	$8p\pi$	3	2.4	26.79	$19p\pi$	4	2.46	5.06	$6p\pi$	8	2.5	19.3
$13p\pi$	0	2.34	7.08	$6p\pi$	4	2.4	43.64	$20p\pi$	4	2.46	5.06	$15p\pi$	6	2.5	8.26
$4p\pi$	4	2.34	66.8	$5p\pi$	5	2.41	32.4	$22p\pi$	4	2.46	4.56	$8p\pi$	7	2.5	13.2
$7p\pi$	1	2.34	19.27	$4p\pi$	7	2.41	43.65	$23p\pi$	4	2.46	4.38	$16p\pi$	6	2.5	5.36
$16p\pi$	0	2.34	4.08	$9p\pi$	3	2.41	17.07	$26p\pi$	4	2.46	3.57	$9p\pi$	7	2.51	13.71
$17p\pi$	0	2.34	3.84	$10p\pi$	3	2.41	16.21	$27p\pi$	4	2.46	3.57	$4p\pi$	12	2.51	20.52
$8p\pi$	1	2.35	19.05	$11p\pi$	3	2.42	15.1	$28p\pi$	4	2.46	3.34	$10p\pi$	7	2.51	13.34
$6p\pi$	2	2.35	37.91	$7p\pi$	4	2.42	27.63	$9p\pi$	5	2.46	16.5	$7p\pi$	8	2.51	17.37
$9p\pi$	1	2.35	14.4	$12p\pi$	3	2.42	10.02	$10p\pi$	5	2.47	15.04	$5p\pi$	10	2.51	19.34
$5p\pi$	3	2.35	43.95	$13p\pi$	3	2.42	10.57	$7p\pi$	6	2.47	25.27	$11p\pi$	7	2.52	8.63
$10p\pi$	1	2.36	12.68	$15p\pi$	3	2.43	9.11	$4p\pi$	10	2.47	26.29	$12p\pi$	7	2.52	9.12
$11p\pi$	1	2.36	11.62	$18p\pi$	3	2.43	8.24	$12p\pi$	5	2.47	20.86	$6p\pi$	9	2.52	16.61
$4p\pi$	5	2.36	58.29	$19p\pi$	3	2.43	12.27	$13p\pi$	5	2.47	10.24	$14p\pi$	7	2.52	7.49
$12p\pi$	1	2.36	10.8	$8p\pi$	4	2.43	34.56	$5p\pi$	8	2.47	28.14	$4p\pi$	13	2.52	17.22
$7p\pi$	2	2.37	26.56	$5p\pi$	6	2.43	45.51	$14p\pi$	5	2.48	8.48	$24p\pi$	7	2.53	7.94
$15p\pi$	1	2.37	6.94	$6p\pi$	5	2.43	8.23	$15p\pi$	5	2.48	10.67	$9p\pi$	8	2.53	8.9
$16p\pi$	1	2.37	6.4	$4p\pi$	8	2.43	32.32	$6p\pi$	7	2.48	20.33	$5p\pi$	11	2.53	23.79
$8p\pi$	2	2.38	23.56	$9p\pi$	4	2.44	17.61	$8p\pi$	6	2.48	13.73	$6p\pi$	10	2.54	15.56
$6p\pi$	3	2.38	40.58	$10p\pi$	4	2.44	15.95	$18p\pi$	5	2.48	5.44	$4p\pi$	14	2.54	12.56
$5p\pi$	4	2.38	40.87	$11p\pi$	4	2.44	16.47	$20p\pi$	5	2.48	4.83	$12p\pi$	8	2.54	6.7
$9p\pi$	2	2.38	16.16	$7p\pi$	5	2.44	23.9	$43p\pi$	5	2.48	7.36	$5p\pi$	12	2.55	15.86
$4p\pi$	6	2.39	51.98	$13p\pi$	4	2.45	10.56	$9p\pi$	6	2.48	12.68	$52p\pi$	8	2.55	5.72
$11p\pi$	2	2.39	13.94	$14p\pi$	4	2.45	9.92	$10p\pi$	6	2.49	14.19	$7p\pi$	10	2.55	10.27
$12p\pi$	2	2.39	16.84	$15p\pi$	4	2.45	10.38	$4p\pi$	11	2.49	26.02	$4p\pi$	15	2.55	10.47
$7p\pi$	3	2.39	25.12	$4p\pi$	9	2.45	44.21	$7p\pi$	7	2.49	19.66	$4p\pi$	16	2.57	14.16
$13p\pi$	2	2.4	9.65	$16p\pi$	4	2.45	10.76	$11p\pi$	6	2.49	10.13	$4p\pi$	17	2.58	9.48

[1] C. Davisson and L. H. Germer, Nature (London) **119**, 558 (1927).

[2] G. P. Thomson and A. Reid, Nature (London) **119**, 890 (1927).

[3] M. Arndt, O. Nairz, J. Vos-Andreae, C. Keller, G. van der Zouw, and A. Zeilinger, Nature (London) **401**, 680 (1999).

[4] S. Gerlich, S. Eibenberger, M. Tomandl, S. Nimmrichter, K. Hornberger, P. J. Fagan, J. Tüxen, M. Mayor, and M. Arndt, Nat. Commun. **2**, 263 (2011).

[5] M. Arndt and K. Hornberger, Nat. Phys. **10**, 271 (2014).

[6] S. Nimmrichter and K. Hornberger, Phys. Rev. Lett. **110**, 160403 (2013).

[7] A. Bassi, K. Lochan, S. Satin, T. P. Singh, and H. Ulbricht, Rev. Mod. Phys. **85**, 471 (2013).

[8] T. Reisinger, A. A. Patel, H. Reingruber, K. Fladischer, W. E. Ernst, G. Bracco, H. I. Smith, and B. Holst, Phys. Rev. A **79**, 053823 (2009).

[9] This, in our terminology, includes the van der Waals force as a special case.

[10] C.-T. Tai, *Dyadic Green Functions in Electromagnetic Theory* (IEEE, New York, 1994).

[11] C. Eberlein and R. Zietal, Phys. Rev. A **86**, 052522 (2012).

[12] T. Reisinger, G. Bracco, and B. Holst, New J. Phys. **13**, 065016 (2011).

[13] B. Derjaguin, Kolloid-Z. **69**, 155 (1934).

[14] S. Buhmann, *Dispersion Forces I: Macroscopic Quantum Electrodynamics and Ground-State Casimir, Casimir–Polder and van der Waals Forces*, Springer Tracts in Modern Physics (Springer, Berlin/Heidelberg, 2013); *Dispersion Forces II: Many-Body Effects, Excited Atoms, Finite Temperature and Quantum Friction*, Springer Tracts in Modern Physics (Springer, Berlin/Heidelberg, 2013).

[15] L. Knöll, S. Scheel, and D.-G. Welsch, QED in dispersing and absorbing dielectric media, in *Coherence and Statistics of Photons and Atoms*, edited by J. Peřina (Wiley, New York, 2001), p. 1.

[16] S. Y. Buhmann, L. Knöll, D.-G. Welsch, and H. T. Dung, Phys. Rev. A **70**, 052117 (2004).

[17] H. Hamaker, Physica **4**, 1058 (1937).

[18] J. D. Perreault, A. D. Cronin, and T. A. Savas, Phys. Rev. A **71**, 053612 (2005).

[19] K. Hornberger, S. Gerlich, P. Haslinger, S. Nimmrichter, and M. Arndt, Rev. Mod. Phys. **84**, 157 (2012).

[20] T. Juffmann, S. Nimmrichter, M. Arndt, H. Gleiter, and K. Hornberger, Found. Phys. **42**, 98 (2012).

[21] T. Reisinger, S. Eder, M. M. Greve, H. I. Smith, and B. Holst, Microelectron. Eng. **87**, 1011 (2010).

[22] T. N. Olney, N. M. Cann, G. Cooper, and C. E. Brion, Chem. Phys. **223**, 59 (1997).

[23] R. D. Johnson III (ed.), *NIST Computational Chemistry Comparison and Benchmark Database Release 18, NIST Standard Reference Database Number 101* (NIST, Gaithersburg, 2016).
[24] R. Brühl, P. Fouquet, R. E. Grisenti, J. P. Toennies, G. C. Hegerfeldt, T. Köhler, M. Stoll, and C. Walter, Europhys. Lett. **59**, 357 (2002).
[25] J. L. Hemmerich, R. Bennett, T. Reisinger, S. Nimmrichter, J. Fiedler, H. Hahn, H. Gleiter, and S. Y. Buhmann, Phys. Rev. A **94**, 023621 (2016).
[26] W. G. Spitzer and D. A. Kleinman, Phys. Rev. **121**, 1324 (1961).
[27] R. E. Grisenti, W. Schöllkopf, J. P. Toennies, G. C. Hegerfeldt, and T. Köhler, Phys. Rev. Lett. **83**, 1755 (1999).
[28] D. E. Dauger, Comput. Phys. **10**, 591 (1996).
[29] The reported wavelength in Ref. [8] was inaccurate and corresponded to the speed from a noncalibrated time-of-flight measurement. We therefore use the more accurate value noted here.
[30] T. Reisinger, P. Leufke, H. Gleiter, and H. Hahn, New J. Phys. **19**, 033022 (2017).
[31] The background I_{BG} and unobstructed intensity I_0 were reported only in approximate fashion. Here we use the following more accurate values determined from the original data files: $b = 321$ mm: $I_{\mathrm{BG}} = (490 \pm 5)\ \mathrm{s}^{-1}$, $I_0 = (4200 \pm 50)\ \mathrm{s}^{-1}$, $I_{\mathrm{PS}} = (523.6 \pm 1.0)\ \mathrm{s}^{-1}$, $I_{\mathrm{rel}} = 0.0091 \pm 0.0014$. $b = 641$ mm: $I_{\mathrm{BG}} = (478 \pm 5)\ \mathrm{s}^{-1}$, $I_0 = (3000 \pm 40)\ \mathrm{s}^{-1}$, $I_{\mathrm{PS}} = (519.3 \pm 2.1)\ \mathrm{s}^{-1}$, $I_{\mathrm{rel}} = 0.0164 \pm 0.0021$. $b = 801$ mm: $I_{\mathrm{BG}} = (463 \pm 5)\ \mathrm{s}^{-1}$, $I_0 = (2600 \pm 40)\ \mathrm{s}^{-1}$, $I_{\mathrm{PS}} = (497.4 \pm 2.9)\ \mathrm{s}^{-1}$, $I_{\mathrm{rel}} = 0.0161 \pm 0.0026$.
[32] T. Reisinger and B. Holst, J. Vac. Sci. Technol. B **26**, 2374 (2008).
[33] T. Reisinger, M. M. Greve, S. D. Eder, G. Bracco, and B. Holst, Phys. Rev. A **86**, 043804 (2012).
[34] M. S. Safronova, U. I. Safronova, and S. G. Porsev, Phys. Rev. A **87**, 032513 (2013).
[35] A. Allison and A. Dalgarno, Mol. Phys. **19**, 567 (1970).
[36] M. Glass-Maujean, A.-M. Vasserot, C. Jungen, H. Schmoranzer, A. Knie, S. Kübler, and A. Ehresmann, J. Mol. Spectrosc. **315**, 155 (2015).